

The assembly of spheroid-dominated galaxies in the EAGLE simulation

M. S. Rosito¹, P. B. Tissera^{2,3}, S. E. Pedrosa¹, Y. Rosas-Guevara^{2,4}

¹ Instituto de Astronomía y Física del Espacio, CONICET-UBA, Casilla de Correos 67, Suc. 28, 1428, Buenos Aires, Argentina.

² Departamento de Ciencias Físicas, Universidad Andrés Bello, 700 Fernandez Concha, Santiago, Chile.

³ Corresponding Investigator, IATE-CONICET, Laprida 927, Córdoba, Argentina.

⁴ Centro de Estudios de Física del Cosmo de Aragón, Plaza San Juan 1, Planta 2, E-44001 Teruel, Spain.

April 29, 2022

ABSTRACT

Context. Despite the insights gained in the last few years, our knowledge about the formation and evolution scenario for the spheroid-dominated galaxies is still incomplete. New and more powerful cosmological simulations have been developed that together with more precise observations open the possibility to study in more detail the formation of early-type galaxies (ETGs).

Aims. The aim of this work is to analyse the assembly histories of ETGs in a Λ -CDM cosmology, focusing on the archeological approach given by the mass growth histories.

Methods. We inspect a sample of dispersion-dominated galaxies selected from the largest volume simulation of the EAGLE project (L100N1504). This simulation includes a variety of physical processes such as radiative cooling, star formation (SF), metal enrichment and stellar and AGN feedback. The selected sample comprised 508 spheroid-dominated galaxies classified according to their dynamical properties. Their surface brightness profile, the fundamental relations, kinematic properties and stellar mass growth histories are estimated and analysed. The findings are confronted with recent observations.

Results. The simulated ETGs are found to reproduce globally the fundamental relations of ellipticals. All of them have an inner disc component where residual younger stellar populations (SPs) are detected. The fraction of this inner disc correlates with bulge-to-total ratio. We find a relation between kinematics and shape which implies that dispersion-dominated galaxies with low V/σ_L tend to have ellipticity smaller than ~ 0.5 and are dominated by old stars. On average, less massive galaxies host slightly younger stars. More massive spheroids show coeval SPs while for smaller galaxies, there is a clear trend to have rejuvenated inner regions. The age gap detected between the inner and the outer regions grows from ~ 0.5 Gyr for massive EAGLE spheroid-dominated galaxies to ~ 2 Gyr for the smaller analysed systems. We find evidences suggesting that both the existence of the discs components with star formation activity in the inner region and the accretion of satellite galaxies in outer regions could contribute to the outside-in formation history. Stronger SN feedback and/or the action of AGN feedback for masses around $10^{10} M_\odot$ could contribute to prevent the SF in the inner regions.

Key words. galaxies: formation – galaxies: elliptical and lenticular, cD – galaxies: abundances – galaxies: kinematics and dynamics

1. Introduction

Once thought as simple systems formed in a monolithic collapse, early-type galaxies (ETGs) are currently considered complex structures formed probably by the combination of diverse physical processes such as infall and collapse, major/minor mergers (e.g. Zavala et al. 2012; Tissera 2012; Perez et al. 2013; Avila-Reese et al. 2014, and references therein). The development of integral field spectroscopy (IFS) has allowed a deeper analysis of the SPs and interstellar medium (ISM) of galaxies and particularly of ETGs. Recent multi-object surveys such as SAMI (Croom et al. 2012) and MaNGA (Bundy et al. 2015; SDSS Collaboration et al. 2016), and single-object ones like ALTA^{3D} (Cappellari et al. 2011) and CALIFA (Sánchez et al. 2012) make it possible to deepen our understanding of the astrophysical properties and fundamental relations of galaxies in a wide range of stellar masses and morphologies.

The construction of stellar mass growth histories (MGHs) for a significant number of galaxies have been made possible by IFS surveys. The MGHs provide a measure of galaxy assembly. Recent observational works find a significant fraction of galaxies

in the Local Universe to be consistent with an inside-out formation history as they exhibit negative age gradients (Wang et al. 2011; Lin et al. 2013; Li et al. 2015). This implies that the SF in the inner regions occurs at earlier time than in outer regions of the galaxies. For the ETGs, it is not yet clear how they assembled and/or quenched their star formation activity as a function of radius. Supernova and AGN feedback can contribute to regulate the star formation activity in galaxies of different masses. Recent results by Argudo-Fernández et al. (2018) suggest that AGN feedback might even act in galaxies with stellar masses down to $10^{10} M_\odot$.

Evidences for both inside-out and outside-in scenarios for ETGs has been reported (Sánchez-Blázquez et al. 2007). Ibarra-Medel et al. (2016) study galaxies from MaNGA survey (Bundy et al. 2015; SDSS Collaboration et al. 2016) finding an inside-out scenario in star-forming and late-type galaxies. In less massive systems, there is a larger variety of behaviours in the observed MGHs. ETGs are detected to be consistent with a weak inside-out formation at later epochs. At early epochs, a slight trend from outside-in formation is found. However, the main caveat to study ETGs assembly is the determination of ages for SPs older than

10 Gyr. Another effect to be considered in the formation of ETGs is the contribution of old stars acquired by satellite accretion (e.g. Genel et al. 2018). The accretion of satellites could add older stars in the outer regions helping to establish an outside-in formation scenario. However, if the accreted SPs are younger than the main SPs of the principal galaxy then the opposite scenario could be set. From an observational point of view, this is yet not clearly established.

The current cosmological scenario for the formation of the structure show that different morphologies can be associated with different formation histories at a given stellar mass (De Rossi et al. 2015; Trayford et al. 2018). In particular, mergers have been shown to be able to change galaxy morphology drastically (e.g. Mihos & Hernquist 1996). During the early stages of the interactions, these processes may trigger tidal fields that drive gas inflows, producing starbursts which can feed the spheroidal component (Hernquist 1989; Sillero et al. 2017). These processes can modify the metallicity distributions, contributing to weaken the metallicity gradients as well as triggering SF (e.g. Rupke et al. 2010; Perez et al. 2013; Tissera et al. 2016; Taylor & Kobayashi 2017; Bustamente 2018). Galactic winds might be generated by stellar/AGN feedback that could transport material out of the galaxy modifying the morphologies, the star formation activity and the chemical abundances (e.g. Gibson et al. 2013; Genel et al. 2015; Dubois et al. 2016). Naab (2013) proposes a two-phase assembly history: dissipative processes with in situ SF at high redshift and then dry accretion of nearby galaxies. Dry mergers have also been proposed as a mechanism responsible for the formation of ETGs, principally of the outskirts, because they contribute with old stars and small amount of gas to fuel new star formation activity (Genel et al. 2018). While SN feedback is a crucial process to regulate the transformation of gas into stars in galaxies, AGN feedback is also required at high stellar masses where SN feedback is not that efficient.

Clauwens et al. (2018) study the origin of the different morphologies in central galaxies from the EAGLE simulation (Schaye et al. 2015; Crain et al. 2015). They describe how the disc and the bulge components of galaxies form. They distinguish three phases of galaxy formation. When $M_{\text{Star}} < 10^{9.5} M_{\odot}$, galaxy evolution would be dominated by random motions, growing disorderly. In this phase, SF occurs mostly in situ, possible fed by wet mergers. When the stellar mass of galaxies is in the range $10^{9.5} M_{\odot} < M_{\text{Star}} < 10^{10.5} M_{\odot}$, there is also in situ SF, but in systems with disc morphologies. Finally, at higher masses, there is a transformation to more spheroid-dominated galaxies where the spheroid formation is mainly due to accretion of ex-situ stars at large radii. Trayford et al. (2018) also analyse the morphological evolution of galaxies in the EAGLE simulation, studying the changes produced by mergers, accretion and secular evolution in galaxies as a function of redshift. They conclude that the mass fraction of spheroids increases steadily towards $z \sim 0$ and that galaxies that have mergers with mass ratios larger than 1 : 10 tend to change their morphology from disc-dominated to spheroidal-dominated.

Recently, Rosito et al. (2018) investigate a sample of field ETGs selected from Fenix project (Pedrosa & Tissera 2015). These authors report the simulated ETGs to be able to reproduce the size-mass relation, fundamental plane (FP) and the Faber-Jackson relation (FJR) and to have formed in an inside-out fashion, in general. All the analysed dispersion-dominated galaxies have small disc components and ~ 60 per cent of them can be classified as pseudo-bulges. These authors find that the spheroidal galaxies have slightly bluer colours than expected, consistent with having been recently rejuvenated. Compared to

observations, the fraction of rejuvenated simulated spheroids is larger, suggesting the need for a stronger quenching mechanism. However, the MGHs obtained by Rosito et al. (2018) are in global agreement with the observational trends by Ibarra-Medel et al. (2016) that shows an inside-out formation history for low-mass galaxies ETGs. For massive ETGs, all SPs seem to be co-eval with a slight trend to inside-out formation. This study is based on a small number sample of galaxies (18) restricted to a typical field region of the universe.

In this paper, we analyse the dispersion-dominated galaxies from the EAGLE project (Crain et al. 2015; Schaye et al. 2015), focusing on the 100 Mpc cubic volume simulation. Hence, we increase the statistical sample and explore a larger variety of assembly histories. The selected EAGLE spheroid-dominated galaxies (hereafter, E-SDGs) sample comprises 508 members resolved with more than 10000 stellar particles. In order to validate the E-SDGs, we estimate their structural and fundamental relations and compare them with observations from ATLAS^{3D} (Capellari et al. 2013a,b). We also calculate the shapes and kinematic properties. Then, the mass assembly histories as well as the metallicity properties are analysed according to stellar galaxy mass and the bulge-to-total mass ratio.

This paper is organised as follows. In Section 2, the main aspects of the EAGLE Project are summarised and we characterise the simulated galaxies via morphological decomposition, the analysis of the surface density profile and the scaling relations. In Section 3 we discuss the relation between shape and kinematics. Section 4 describe the MGHs. Finally, Section 5 summarises the results.

2. The EAGLE simulation

We analyse galaxies selected from the 100 Mpc sized box reference run of the EAGLE Project, a suite of hydrodynamical simulations that follow the formation of structure in cosmological representative volumes consistent with the current favoured Λ -CDM cosmology (Crain et al. 2015; Schaye et al. 2015). These simulations include: radiative heating and cooling (Wiersma et al. 2009), stochastic SF (Schaye & Dalla Vecchia 2008) and stochastic stellar feedback (Dalla Vecchia & Schaye 2012). These simulations also include AGN feedback (Rosas-Guevara et al. 2015). The AGN feedback is particular important for the evolution of star formation activity in massive ETGs. An Initial Mass Function (IMF) of Chabrier (2003) is used. A more detail description of the code and the simulations is given by Crain et al. (2015) and Schaye et al. (2015).

The adopted cosmological parameters are: $\Omega_m = 0.307$, $\Omega_{\Lambda} = 0.693$, $\Omega_b = 0.04825$, $H_0 = 100 h \text{ km s}^{-1} \text{ Mpc}^{-1}$, with $h = 0.6777$ (Planck Collaboration et al. 2014a,b). The 100 Mpc sized box reference simulation, so called L100N1504, is represented by 1504^3 dark matter particles and the same initial number of gas particles, with an initial mass of $9.70 \times 10^6 M_{\odot}$ and $1.81 \times 10^6 M_{\odot}$, respectively (Schaye et al. 2015). A maximum gravitational softening of 0.7 kpc is adopted.

2.1. The selected sample of galaxies

In this work, we use the sample of 7000 central galaxies selected by Tissera et al. (2018) from the EAGLE galaxy catalog of L100N1504. To diminish numerical resolution artefacts, we only analyse those galaxies resolved with more than 10000

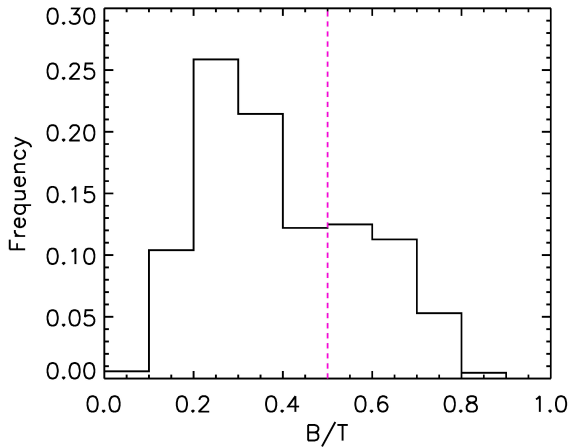


Fig. 1. Distribution of the B/T ratios for the selected simulated galaxies. Only those galaxies with $B/T > 0.5$ are classified as SDGs (magenta dashed line).

stellar particles within $1.5 R_{\text{opt}}$ ¹. Thus, the selected EAGLE galaxy subsample has 1721 members with masses in the range $\sim [0.22 - 16.7] \times 10^{10} M_{\odot}$.

The morphological classification is performed by applying the method described by Tissera et al. (2012). For each particle, we use the parameter $\epsilon = J_z/J_{z,\text{max}}(E)$. J_z is the angular momentum component in the direction of the total angular momentum and $J_{z,\text{max}}$ is the maximum J_z over all particles at a given binding energy (E). Those particles with $\epsilon > 0.5$ are associated with the disc component, whereas the rest of them are considered part of the spheroid component. In order to discriminate between the bulge (also called spheroid) and the stellar halo, the particle binding energy is used so that the most bounded particles belong to the spheroid. We assume the minimum energy of the particles at half of R_{opt} as the threshold (Tissera et al. 2012).

This decomposition allows the definition of the bulge-to-total mass ratios (B/T), which are used to select galaxies according to their morphology. In Fig. 1, we show the distribution of B/T ratios for our EAGLE sample. Following previous works, (Pedrosa & Tissera 2015; Rosito et al. 2018; Tissera et al. 2018), we adopt $B/T = 0.5$ to separate disc-dominated from spheroid-dominated galaxies (DDGs and SDGs, respectively).

The SDG sample comprises 508 members and will be hereafter called E-SDGs. As can be seen from Fig. 1, all simulated galaxies have a stellar disc component, regardless of the size of spheroidal system. The total stellar masses of the E-SDGs defined as the sum of the bulge and disc stellar mass components within $1.5 R_{\text{opt}}$ are in the range $[0.4, 14] \times 10^{10} M_{\odot}$. We also estimate the stellar half-mass radius, R_{hm} , as the one that encloses 50 per cent of the total stellar mass.

For each E-SDG, we measure the specific star formation rate (sSFR), the median stellar age, the central velocity dispersion (σ), the rotational velocity (V) and the chemical abundances: $[\text{Fe}/\text{H}]$, $[\text{O}/\text{Fe}]$ and $[\text{O}/\text{H}]$ of the SPs.

In the rest of this section, we analyse the structural parameters and fundamental relations determined by the E-SDGs and compare them with observations.

2.1.1. Surface mass densities

The projected stellar-mass surface density profiles for both disc and spheroid components are estimated. Sérsic profiles (Sérsic 1968) are fitted for the bulges, obtaining the central surface brightness (I_0), the scale radius (R_b) and the so-called Sérsic index (n) according to

$$I(R) = I_0 \exp(-(R/R_b)^{1/n})$$

The surface density profiles of the discs are fitted with an exponential profile ($n = 1$) with a scale-length R_d .

We consider the projected stellar-mass surface density as a proxy of the luminosity surface brightness, which is equivalent to adopting a mass-to-light ratio $M/L = 1$. This ratio is close to the observed one for the infrared bands and is consistent with that adopted by Rosito et al. (2018).

In the case of the spheroidal components, the Sérsic profile is fitted within the radial range defined by one gravitational softening and the radius that encloses 90 per cent of the total spheroid mass (to avoid numerical noise in the inner and very outer regions). The exponential fit to the discs is performed within the latter and the R_{opt} .

In Fig. 2, we show two examples of simulated galaxies with different surface density profiles. As can be seen, the profiles are well-reproduced by the Sérsic law and an exponential profile for the spheroid and disc, respectively. In the central regions, the bulge and disc components co-exist, although different behaviours are identified as can be seen from Fig. 2. In general, the discs either extend into the bulge region, following the disc exponential profiles (upper panel) or increase their surface density so that they might reach that of the bulge (lower panel). The different characteristics of the co-existence of the discs and the spheroids reflect the variety of assembly histories (e.g. Trayford et al. 2018).

Following Rosito et al. (2018), we quantify the fraction of the disc stellar mass that co-exists with the bulge component by estimating the stellar mass with $\epsilon > 0.5$ and binding energy lower than the energy threshold adopted to define the bulges (F_{rot}). In Fig. 3 we show F_{rot} as a function of B/T . In order to obtain smoothed distributions, we use the Python implementation (Cappellari et al. 2013b) of the two-dimensional Locally Weighted Regression (Cleveland & Devlin 1988) method. This method generalizes the polynomial regression and has the advantage that it is not necessary to specify a function to fit a model to the data sample, being notably simply to implement. By smoothing our plots, the tendencies can be more clearly appreciated. We must bear in mind, however, that some colours may be affected by this method. We apply this method in all our scatter plots, hereafter. In Appendix B we include the figures without smoothing the distributions. We fix the colorbar limits to the first and third quartile of the variable according to which we colour the symbols in the smoothed plots, except for the ones in Appendix A.

Most of the E-SDGs (~ 85 per cent) have $n < 2$ (~ 53 per cent of the E-SDGs have $n > 1$) and will be classified as pseudo-bulges. These systems are expected to have been formed by a significant contribution of secular evolution (see Kormendy 2016, for a recent review). We note that other authors assumes different definitions taken into account, for example, the inner shape or just the resulting product of secular evolution in the inner part of the galactic disc (e.g. Falcón-Barroso & Knapen 2012; Gadotti 2009).

¹ The optical radius, R_{opt} , is defined as the one that encloses ~ 80 per cent of the baryonic mass (gas and stars) of the galaxy (Tissera 2000). This definition allows a determination of a characteristic radius that adapts to the size and mass distribution of a given galaxy.

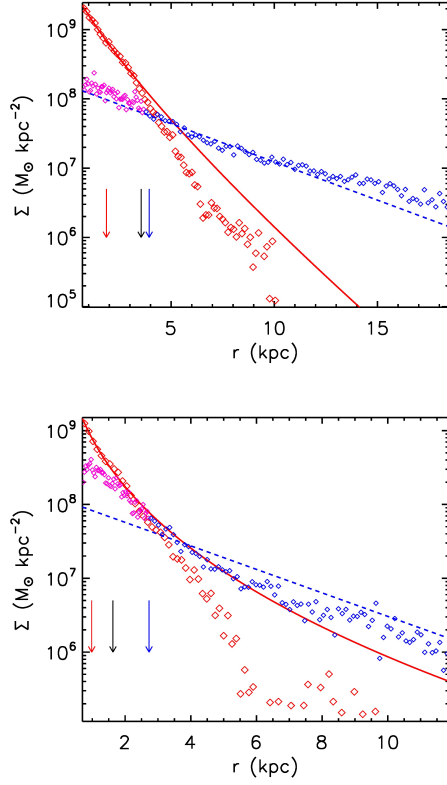


Fig. 2. The projected stellar mass surface density profiles for the bulge (red diamonds) and disc components (blue diamonds) of two typical simulated ETGs. The regions of the discs that coexist with spheroidal components are highlighted (magenta diamonds). The best-fitted Sérsic profiles for the spheroidal components (red solid lines) and the exponential profiles for the discs (blue dashed lines) are also included. The bulge effective radius (R_{eff} , calculated by using equation 6 in Sáiz et al. 2001), the R_{hm} and the R_d are depicted with red, black and blue arrows, respectively. In the upper panel, the inner disc follows the exponential profile ($n \sim 1.25$) while in the lower panel, the same component follows the bulge profile ($n \sim 2.78$). A variety of behaviours is detected, suggesting different contributions of processes such as collapse, mergers and secular evolution.

As can be seen from Fig. 3, E-SDGs with large B/T ratios tend to have small F_{rot} . This is the expected behaviour considering that more massive galaxies have larger probability to have experienced massive mergers that could destroy the discs, producing more classical bulges (Clauwens et al. 2018; Correa et al. 2018). There is only a weak trend to have slightly higher n for these galaxies. On the other hand, larger inner discs ($F_{\text{rot}} > 0.2$) are found in the more discy E-SDGs that tend to have $n \leq 1$, as expected if bulges formed from secular evolution. As can be seen from this figure, at a given B/T ratio, there is a large variation of F_{rot} , suggesting different assembly histories (i.e. different contributions of collapse, mergers and secular evolution for example). There is no clear trend for galaxies with $n > 2$ as can be seen from the inner set of Fig. 3, where the distribution has not been smoothed. The Spearman coefficient for the relation is -0.47 . The linear regression yields a slope of -0.40 ± 0.04 (this error is calculated by a bootstrap method). The relation suggests that those galaxies that have larger disc components are able to extend these discs all the way to the central region (Rosito et al. 2018).

The E-SDGs show no clear correlation between B/T and n as shown in Fig. 4 (Spearman coefficient 0.09, p-value of

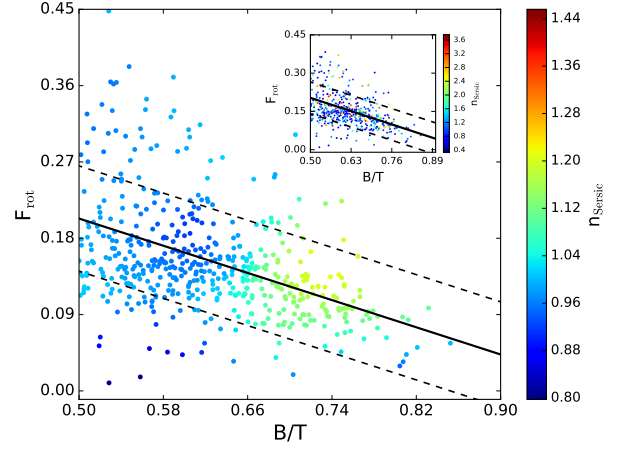


Fig. 3. Stellar-mass fractions F_{rot} of the discs that co-exist with the spheroidal components as a function of the B/T ratio. Symbols are coloured according to n . A linear regression fit is included (black solid line) along with its 1σ dispersion (black dashed lines). In the inset plot, we show the same relation without smoothing the distribution of n .

0.03). Gadotti (2009), who finds pseudo-bulges with $n > 2$ by analysing their mean surface brightness as a function of the effective radius, concludes that these kind of bulges do not follow a correlation between B/T and n . Thus, we agree with them in the sense that most of the E-SDGs can be considered pseudo-bulges. From Fig. 4, we can also see that those E-SDGs with larger B/T ratios have, on average, the oldest SPs (E-SDGs galaxies are coloured according to mass-weighted average age of the total galaxy). We note that the E-SDGs with the larger n index tend to have slightly younger SPs, on average. This is because there is a larger fraction of young stars associated to the disc components as we will discuss in more detail in Section 4.

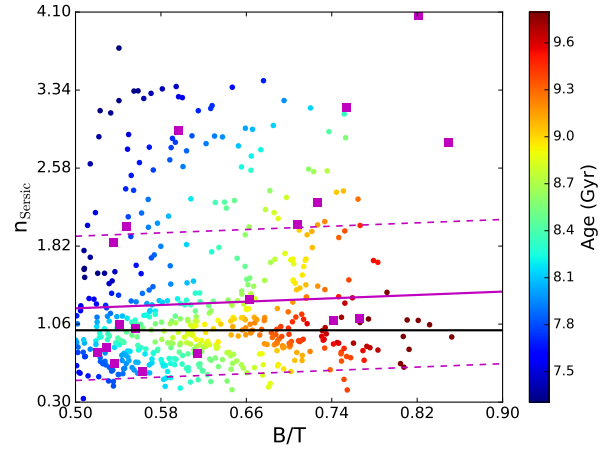


Fig. 4. The Sérsic index (n_{Sersic}) as a function of B/T ratio for the simulated E-SDGs, coloured according to the mass-weighted average age of the galaxy stellar mass. A linear regression fit is included (magenta solid line) with its 1σ dispersion (magenta dashed line). For comparison, we also include the results by Rosito et al. (2018) (magenta squares). The line $n_{\text{Sersic}} = 1$ is depicted in a black line. See Appendix B for the non-smoothed distribution.

In Fig. 5, we show the mean mass-weighted ages as a function of the stellar mass for the E-SDGs. The color code denotes the B/T ratios. As can be seen, there is a general trend to have more massive galaxies populated by old stars, on average, and

with larger B/T ratios as expected. As one moves to more discy E-SDGs, the stellar ages are smaller and the galaxies are less massive. However, note that at a given stellar mass, there is a large variety of morphologies and ages.

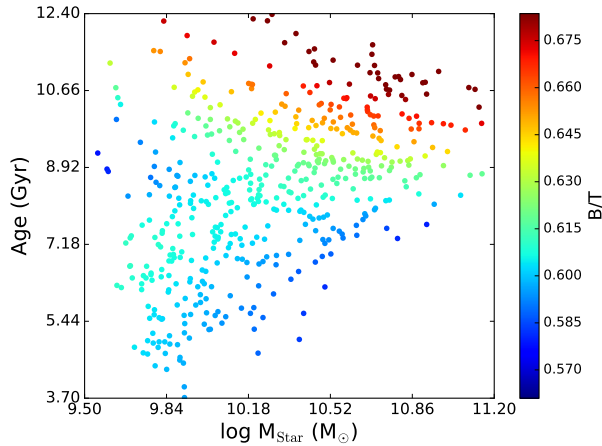


Fig. 5. Mass-weighted average stellar age of the E-SDGs (i.e. bulge and disc SPs) as a function of stellar mass for the simulated galaxies. The symbols are coloured according to the B/T ratios. See Appendix B for the non-smoothed distribution.

2.1.2. Scaling relations

In this subsection, we analyse three main scaling relations for the E-SDGs: the size-mass relation, the FJR (Faber & Jackson 1976) and the FP (Faber et al. 1987; Dressler et al. 1987; Djorgovski & Davis 1987), and compare them with observations. To estimate these scaling relations we use the R_{hm} as the characteristic size for the simulated galaxies.

Size-Mass relation

The size-mass relation for the E-SDGs and the one obtained from different observations are shown in Fig. 6. We compare simulated size-mass relation with the observational trends reported by Mosleh et al. (2013) and Bernardi et al. (2014). For the former, we take those corresponding to ETGs (table 1 in Mosleh et al. 2013) and for the latter, we choose the case of a single Sersic profile (their table 4). We also compare our results with the observations from ATLAS^{3D} Project that consists of a sample of 260 nearby ETGs (Cappellari et al. 2011, 2013a). The stellar masses are calculated from the luminosities given by Cappellari et al. (2013a, table1) and by using the mass-to-light ratios of Cappellari et al. (2013b, table1) for a Salpeter IMF (Salpeter 1955). The corresponding correction to transform Salpeter estimated stellar masses to the Chabrier IMF (Chabrier 2003) is applied.

As can be seen in Fig. 6, E-SDGs within given B/T ratios are located on particular tracks, showing a correlation in agreement with observations albeit shallower (see also Rosito et al. 2018). There is a systematic variation of sizes as a function of B/T at a given stellar mass. E-SDGs with $B/T \geq 0.6$ are in better agreement with the observed relation from ATLAS^{3D}. E-SDGs with smaller B/T ratios are displaced to larger R_{hm} ; they are more consistent with the relation for late-type galaxies (e.g. Mosleh et al. 2013). This is consistent with the existence of larger disc

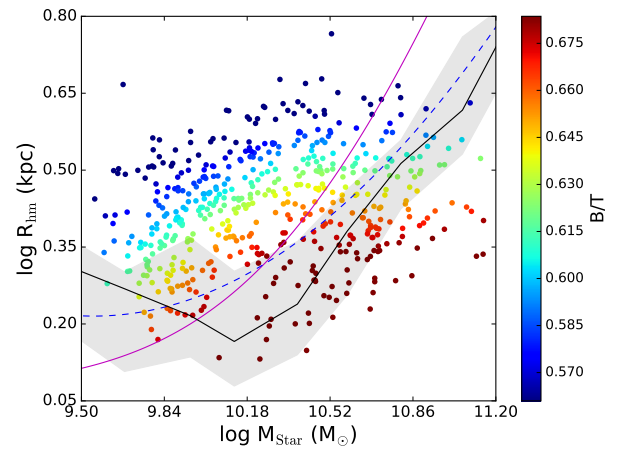


Fig. 6. The mass-size relation estimated for the E-SDGs. Symbols are coloured according to their B/T ratio. The median of the observations from ATLAS^{3D} (black line; the first and third quartiles are shown as shadowed region) and the observed relations for ETGs reported by Mosleh et al. (2013, magenta solid line) and Bernardi et al. (2014, blue dashed line) are included for comparison. See Appendix B for the non-smoothed distribution.

components in the central region that contribute to radially expand the stellar distributions, as shown in Fig. 3.

The Faber-Jackson relation

The FJR links kinematic and photometric properties: $L \propto \sigma^\gamma$, where L is the luminosity and σ the velocity dispersion. The observational results from Cappellari et al. (2013a) are used to confront the simulated relations. We estimate the FJR by adopting a mass-to-light ratio (M/L) and by estimating the dynamical mass (M_{dyn}) using σ within the R_{hm} (σ_e) similarly to the observational procedure. In the first case, a $M/L = 0.5$ for the E-SDGs to convert stellar masses into luminosities is adopted as shown in the upper panel of Fig. 7. The E-SDG FJR has a slope of 0.33 ± 0.01 , which is in agreement with that obtained from ATLAS^{3D}, 0.34 ± 0.02 (the errors are calculated by a bootstrap method). The simulated FJR using the dynamical mass is shown in the lower panel of Fig. 7. As can be seen, E-SDGs follow the expected trend with more massive galaxies to have larger dispersion velocities. In this case we obtained a FJR with a slope of 0.40 ± 0.01 . The difference in the slopes could be due to a different fraction of dark matter in the simulations. In fact, the comparison of both relations suggests that massive E-SDGs might have slightly less dark matter in the central regions than estimated from observations.

The fundamental plane

The FP (Faber et al. 1987; Dressler et al. 1987; Djorgovski & Davis 1987) links the size (R_{eff}) with the luminosity surface density (Σ_e) and the velocity dispersion (σ_e):

$$R_{\text{eff}} \propto \sigma_e^\alpha \Sigma_e^\beta$$

We confront the simulated relation with that reported by the ATLAS^{3D} Project with the observed parameters: $\alpha = 0.98$ and $\beta = -0.74$. In Fig. 8, we show the FP for the E-SDGs calculated with those parameters. As can be appreciated from this figure, there is a good agreement with the one-to-one relation for the E-SDGs: the r_{ms} is ~ 0.16 and ~ 0.17 for the least squares regres-

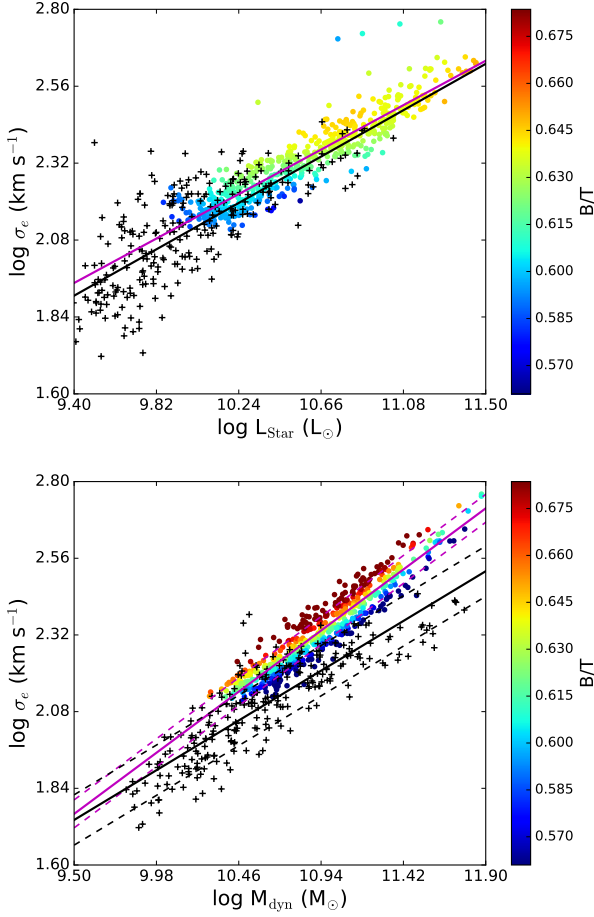


Fig. 7. FJR for simulated E-SDGs (filled circles) and observed ETGs from ATLAS^{3D} (black crosses) galaxies. The upper panel shows the FJR as a function of luminosity and the lower panel as a function of M_{dyn} . The E-SDGs are coloured according to their B/T ratios. The best-fitted linear regressions for the E-SDGs (magenta line) and for the observations (black line) are included. See Appendix B for the non-smoothed distributions.

sion and the one-to-one relation, respectively. However, there is a group of E-SDGs that lies above the plane. They seem to have smaller R_{hm} than expected from observations.

It can be appreciated that, at a given R_{hm} , there is a large dispersion. The zero point of the observed FP is reproduced by assuming $M/L = 1$. Here there is a discrepancy with that required to reproduce the FJ relation, that was well-defined by adopting $M/L = 0.5$.

E-SDGs have been coloured according to the B/T ratios. As can be seen from Fig. 8, E-SDGs with larger B/T ratios are more compact. Considering Fig. 7, they are also more massive.

3. Shape and kinematics

In this section, we now focus on the core aspect of our study: the intrinsic properties of the E-SDGs and their history of assembly. In order to analyse the relation between shape and kinematics, we calculate the V/σ_L ratio where V is the average rotational velocity of the SPs within the R_{hm} and σ_L is the one dimensional velocity dispersion. We assume the velocity dispersion to be isotropic in order to derive σ_L from the 3D σ . The ratio V/σ_L provides a measure of the relative importance of ordered rotation with respect to velocity dispersion (e.g. Dubois et al. 2016).

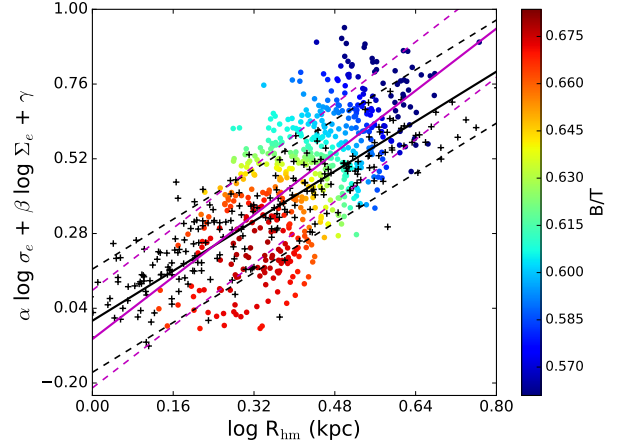


Fig. 8. The FP for the simulated SDGs calculated with the parameters estimated for the ATLAS^{3D} sample. E-SDGs are also depicted according to their B/T ratio. The black line denotes the one-to-one relation and the magenta line represents the best fit for the E-SDGs. In dashed lines we show the rms corresponding to the least squared regression and the one-to-one relation. See Appendix B for the non-smoothed distribution.

For the analysed E-SDGs, a maximum V/σ_L estimated is ~ 1.1 whereas a maximum V/σ_L obtained considering the whole sample (i.e. E-SDGs and E-DDGs) is $V/\sigma_L \sim 2.4$.

The shape of the E-SDGs are determined by fitting ellipsoids to the 3D stellar distributions (as described in Tissera et al. 2010). For each galaxy, we estimate the semiaxis of the ellipsoids as $a \geq b \geq c$ within R_{hm} . The ellipticity is hereafter defined as $\varepsilon = 1 - \frac{b}{a}$. Hence, values of ε close to 1 refer to galaxies that tend to be prolate while galaxies $\varepsilon \sim 0$ are more oblate.

In Fig. 9, we show the V/σ_L versus ε . The observed galaxies from ATLAS^{3D} (Emsellem et al. 2011) and the simulated ones are located in similar regions of this plane. From Fig. 9, we can see that the galaxies with the oldest SPs tend to be more prolate and massive. This trend is in global agreement with the results reported by van de Sande et al. (2018). We also find some massive E-SDGs with high V/σ_L and old SPs in agreement with Lagos et al. (2018) and Cappellari (2016). As can be seen in the bottom panel of this figure, galaxies with high values of B/T tend to have low V/σ_L . Therefore, hereafter, we will define as fast rotators those galaxies with $B/T > 0.7$ and the rest will be considered slow rotators motivated by this trend.

4. Mass growth histories

We investigate the global and radial archaeological MGHs of the E-SDGs. The MGHs are constructed by using the age distribution of the stellar particles at $z \sim 0$. Three radial bins are defined $[0, 0.5]$, $[0.5, 1]$ and $[1, 1.5]$ of R_{hm} , following the observational study of MaNGA galaxies by Ibarra-Medel et al. (2016). We estimate the MGH of each of the 508 E-SDGs.

For this analysis, the E-SDGs are divided in six subsamples. First, we distinguish them according to their stellar masses, defining three subsamples with similar number of galaxies (~ 33 per cent of the total in each one). The mass ranges of the subsamples are given in Table 1. Within each mass subsample, B/T ratios are used to group them according to their morphology: $0.5 < B/T < 0.7$ (hereafter, fast rotators) and $B/T > 0.7$ (hereafter, slow rotators) consistently with Fig. 9 (bottom panel).

We calculate the averaged global and radial MGHs for each group as done in Rosito et al. (2018). These averaged MGHs are

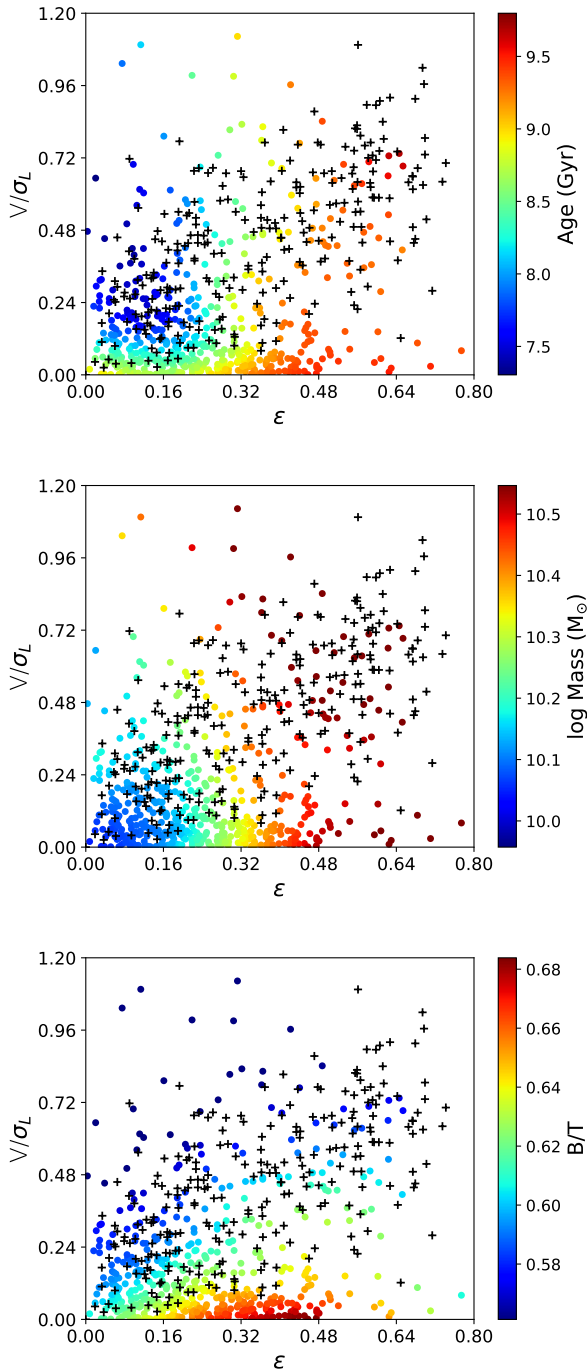


Fig. 9. Anisotropy diagram for the E-SDGs. E-SDGs are coloured according to mass-weighted average age (top panel), stellar mass (middle panel) and B/T ratio (bottom panel). Observational data from ATLAS^{3D} are also shown (Emsellem et al. 2011, black crosses). See Appendix B for the non-smoothed distributions.

normalised to the total mass in each bin (M_0) at a lookback time of 0.5 Gyr in order to have a better comparison with observations (Ibarra-Medel et al. 2016). They are shown in Fig. 10. As can be seen from this figure, massive galaxies (upper panels) show very similar MGHs for each radial interval, implying a more coeval formation history, on average. However, there is a slight trend for the stars in the inner radial bin to be slightly younger. In order to quantify these trends we define the lookback time T^{70} at which 70 per cent of the stellar mass is already formed. Slow

rotators have older star populations by about ~ 0.5 Gyr than fast rotators as indicated by comparing the T^{70} shown in (Table 1). The MGH of massive galaxies are in agreement with results by Ibarra-Medel et al. (2016).

For less massive galaxies, the signals for an overall outside-in formation become stronger, regardless of the B/T ratio. The time T^{70} moves systematically to earlier values so that the smaller galaxies assembled their 70 per cent inner mass at $T^{70} \sim 5 - 6$ Gyr, on average. Low mass E-SDGs show a clear trend from an outside-in formation. In Table 1, we show the T^{70} for each subsample. By taking the difference between T^{70} of the inner and intermediate radial bins for each galaxy, we estimate that about 80 per cent of the E-SDGs are consistent with a outside-in formation. Nevertheless, it is important to note that dispersion in the MGHs is quite large for all analysed subsamples.

The younger populations identified in the central regions could be associated to secular evolution or/and wet minor merger of smaller systems. The MGHs of galaxies with $M_{\text{Star}} < 10^{10.46} M_{\odot}$ show features (i.e. bumps) consistent with the presence of mergers.

The outside-in formation trends are at odds with the results by Ibarra-Medel et al. (2016) for small stellar mass galaxies². Note, however, that there are larger uncertainties in the observational determination of ages. This is particularly important for SPs older than ~ 7 Gyr. Previous results by Rosito et al. (2018), using galaxies selected from Fenix project (Pedrosa & Tissera 2015), show an overall inside-out formation for SDGs in agreement with the results of Ibarra-Medel et al. (2016).

Our findings suggest the existence of discs, particularly, in low-mass galaxies. These discs could have formed as a results of low efficient transformation of gas into stars at higher redshift. The available gas could set on disc structures and feed new SF in the central region via secular evolution. Mergers could also bring in gas that trigger new star formation activity. In that case the younger stars that rejuvenate the central regions of E-SDGs should be associated to the disc components. To test this, the MGHs for the bulge and disc components are estimated separately as shown in Fig. 11. As bulges are smaller, we consider only two radial bins whereas for the disc components, we use the same bins mentioned above.

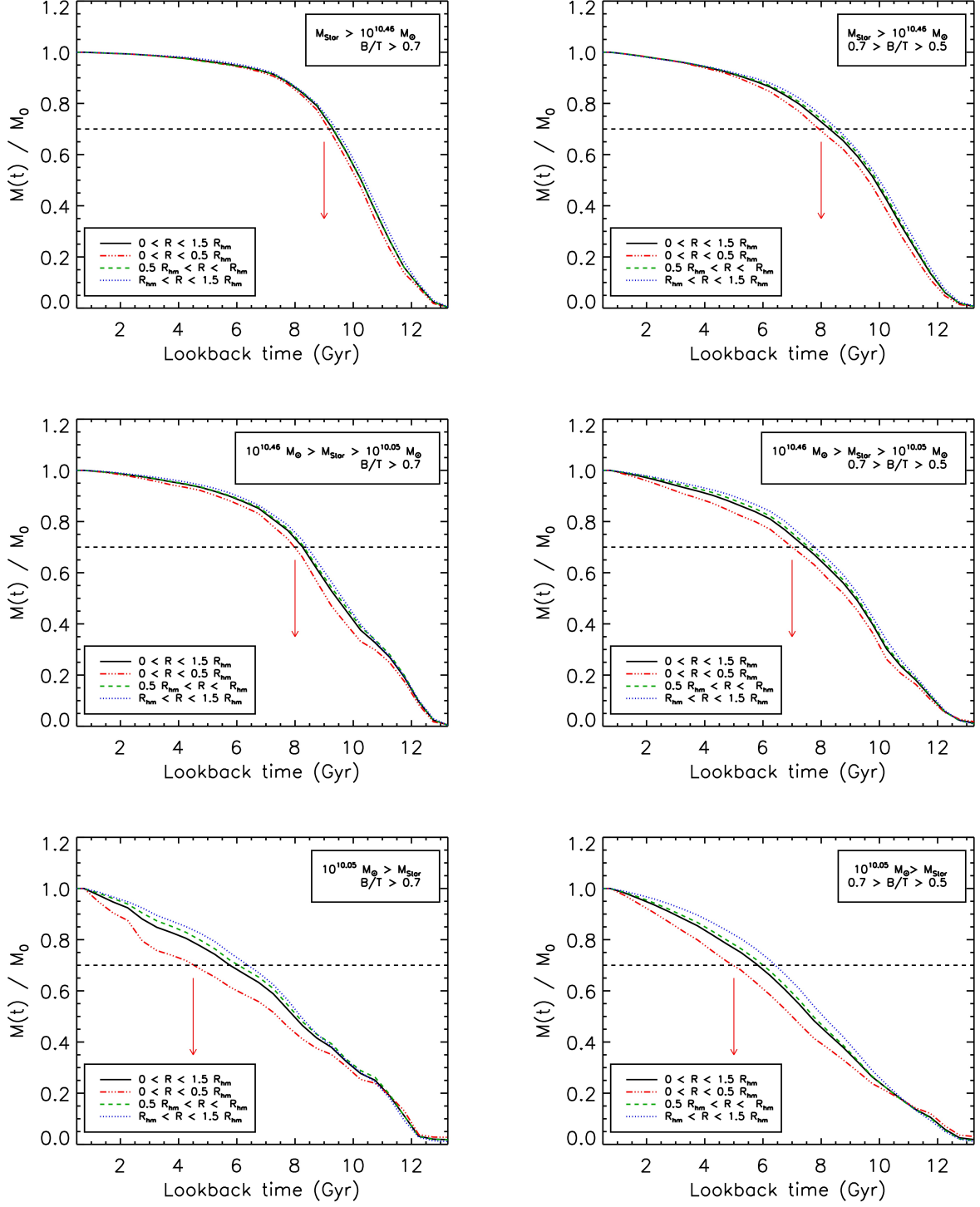
As can be seen from Fig. 11, regardless of mass or B/T ratios, the inner regions of the disc components of the E-SDG are younger, on average. Our results agree with recent findings by Trayford et al. (2018) who show that the star formation activity is associated to the disc components in ETGs in the EAGLE simulations. We go further in this analysis and identify that this SF activity is located mainly in the central regions contributing to rejuvenate the SP and to determine an outside-in formation history of the E-SDGs.

The trends discussed before are averaged behaviours. The complexity of the formation processes of spheroidal galaxies is reflected in the diversity of features and assembly histories (see e.g. Brooks & Christensen 2016; Kormendy 2016, for recent reviews). To illustrate this, Fig. 12 shows the MGHs of two typical E-SDGs with an inside-out (upper, left panel) and an outside-in (upper, right panel) growth. These two galaxies have similar B/T ratios but the first one is more massive (i.e. $M_{\text{Star}} \sim 8.2 \times 10^{10} M_{\odot}$ and $M_{\text{Star}} \sim 4.5 \times 10^{10} M_{\odot}$, respectively). The galaxy that formed outside-in shows a larger inner disc fraction (~ 0.15 for the outside-in and ~ 0.07 for the inside-out

² In the Appendix, we show that DDGs selected from the same simulation have, on average, an inside-out formation (Fig A.2) as reported by previous work (Zavala et al. 2016; Tissera et al. 2018).

Table 1. T^{70} (Gyr) for SPs in each radial bin for galaxies grouped according to their stellar masses M_{Star} (in units of M_{\odot}).

	$10^{10.46} < M_{\text{Star}} < 10^{11.15}$		$10^{10.05} < M_{\text{Star}} < 10^{10.46}$		$10^{9.56} < M_{\text{Star}} < 10^{10.05}$	
	$B/T > 0.7$	$0.5 < B/T < 0.7$	$B/T > 0.7$	$0.5 < B/T < 0.7$	$B/T > 0.7$	$0.5 < B/T < 0.7$
$0 < R < 0.5R_{\text{hm}}$	9.0	8.0	8.0	7.0	4.5	5.0
$0.5R_{\text{hm}} < R < R_{\text{hm}}$	9.5	8.5	8.5	7.5	6.0	6.0
$R_{\text{hm}} < R < 1.5R_{\text{hm}}$	9.5	8.5	8.5	8.0	6.5	6.5


Fig. 10. Average global and radial normalised MGH for the E-SDGs: massive galaxies (top panels), intermediate mass galaxies (middle panels), and low mass galaxies (lower panels). Each group is subdivided according to the B/T ratio: fast rotators (left panels) and slow rotators (right panels). The red arrows point out the lookback time at which 70 per cent of the stellar mass in the inner bin is attained.

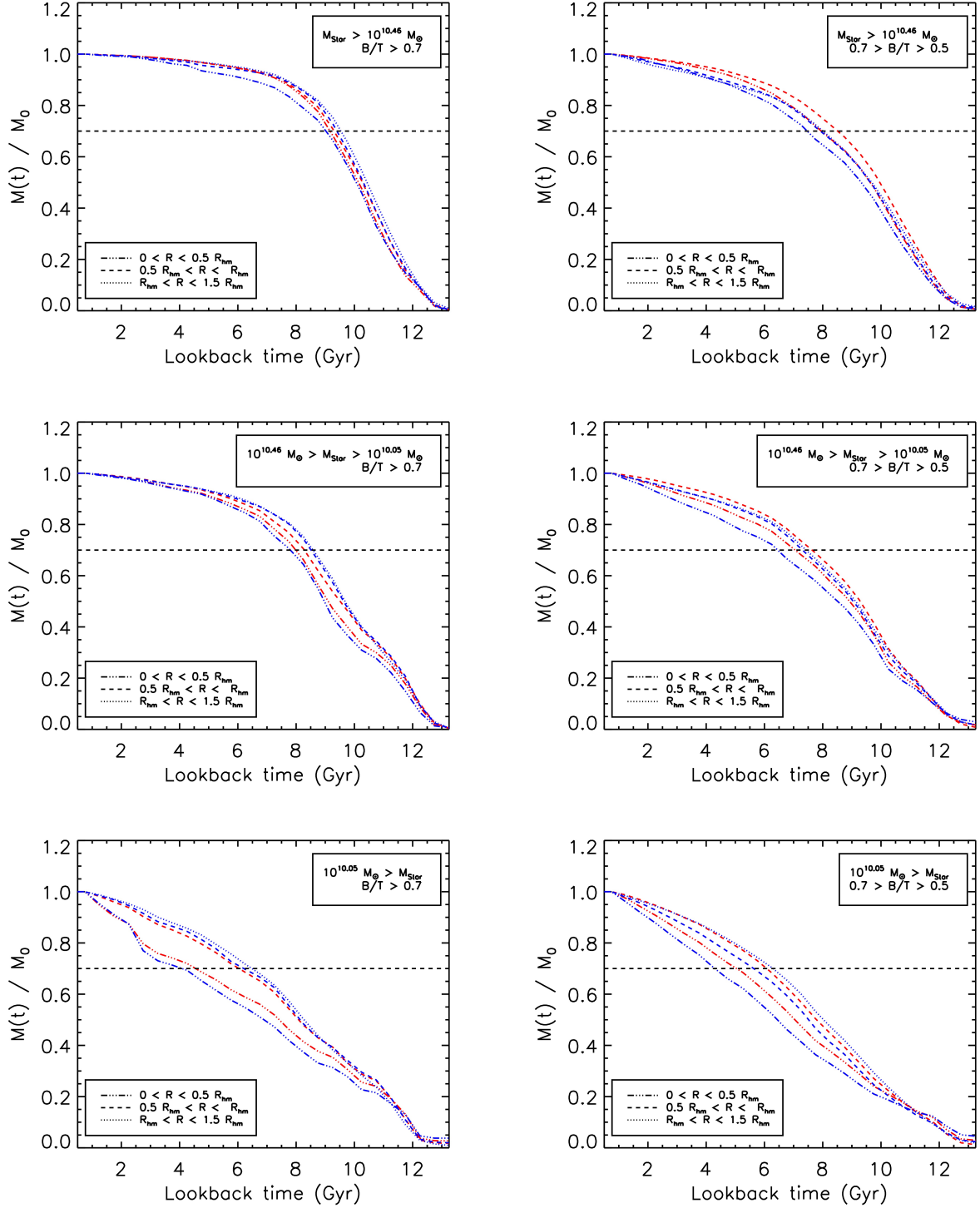


Fig. 11. Radial MGHs for both the bulge (red lines) and the disc (blue lines) components of the E-SDGs: massive galaxies (top panels), intermediate mass galaxies (middle panels), and low mass galaxies (lower panels). Each group is subdivided according to the B/T ratio: fast rotators (left panels) and slow rotators (right panels).

galaxy). In general, galaxies with an outside-in behaviour tend to have slightly larger inner discs: the first and third quartiles of these fractions are 0.11 and 0.18 respectively, whereas the corresponding ones for inside-out galaxies are 0.11 and 0.15 respectively. Both MGHs show signature of strong starbursts that could have been fed by gas-rich mergers. From this figure, we can also see that bumps are present at all defined radial intervals, suggest-

ing that mergers could be the main channel of gas fuelling since they can affect the inner and the outer parts of galaxies (Sillero et al. 2017).

The exploration of the merger trees shows that both have the last mergers event at about 8 – 8.5 Gyr ago but the galaxy with the outside-in formation had a massive merger (1:4) while the galaxy with the inside-out formation had a minor merger

(1:10). McAlpine et al. (2018) show that massive mergers are efficient mechanisms to trigger the rapid growth of the central black hole and the triggering of AGN feedback. The outside-in formation that we detect in the E-SDGs, particularly for low mass galaxies might suggest that the SN feedback is not efficient enough to quench the SF and/or that AGN feedback might be needed even in galaxies of about $10^{10}M_{\odot}$ (Argudo-Fernández et al. 2018).

4.1. Bulge and disc global properties

To gain more insight in this outside-in behaviour, we explore the global properties, ages and star formation efficiency of the bulge and disc components of these galaxies separately.

In Fig 13 we show the mean stellar ages for the spheroid and the disc components in E-SDGs (see Appendix A for the relation for DDGs). As can be seen, the bulge and the disc have similar median ages. For both of them there is a correlation with stellar mass so that the more massive galaxies are dominated by the older SPs (conversely, the DDGs show a clear age difference between the bulge and the discs, so that the SPs in the bulges are systematically older by at least 1.5-2 Gyr in comparison to those of the discs, Fig. A.1 as shown in the Appendix).

The star formation efficiency of the bulge and the disc components show similar trends with galaxy mass as shown in Fig. 14, although the disc components show systematically larger sSFR as expected. Smaller galaxies have slightly stronger star formation activity.

4.2. Chemical abundances

Our analysis indicated that the outside-in behaviour is triggered by stars that are formed in the inner region at later time. If these stars are created from enriched gas by earlier SPs, then they could have different chemical abundances. Hence, we investigate their chemical abundances at different radial distances and in relation with their ages. In Fig. 15, the distribution of the median [O/Fe] and median [Fe/H] for the SPs of the E-SDGs as a function of median age of their SPs are shown.

The median abundances are estimated by using the individual values for each single SP (i.e. represented by a star particle) within the R_{hm} . Hence, the SPs in the very outer regions are not included.

Overall, stars in the E-SDGs are α -enhanced as expected. The [O/Fe] decreases with increasing [Fe/H]. As can be seen from this figure, massive galaxies dominated by old stars have [Fe/H] in the range $[-0.6, -0.2]$ dex and are α -enriched (see also Vincenzo et al. 2018). This is consistent with the fact that more massive galaxies tend to form stars in strong starbursts that also quenched the subsequent SF (via stellar or AGN feedback). E-SDGs with younger stars are distributed in a type of U-shape: those with higher [O/Fe] are located at low metallicities while poor- α systems move to higher metallicities. These trends are consistent with a larger variety in assembly histories for smaller galaxies and star formation activity.

In Fig. 16 we show the distributions of [O/Fe] and [Fe/H] calculated within each radial bin considered in Fig. 10. There is a slight trend for lower [O/Fe] at low [Fe/H] for SPs in the inner radial bin. This suggests that a fraction of the inner stars formed from pre-enriched material compared to the outer parts. From this plot, we can also see that the outer radial regions have a larger contribution of old and α -rich stars. These behaviours could be explained by the later accretion of gas into the cen-

tral regions via secular evolution and/or the contribution of old, high α -enriched stars acquired by accretion of small satellites (Clauwens et al. 2018).

5. Conclusions

We have performed a comprehensive study of a sample of well-resolved numerical spheroid dominated galaxies from the EA-GLE simulation and confront the features and behaviours of these systems with previous results. A galaxy is considered a SDG if $B/T > 0.5$.

We find the following results:

- (i) In agreement with Rosito et al. (2018), all E-SDGs are found to host disc component. Part of these discs co-exists with the bulge. The mass fraction of inner disc over the bulge anti-correlates with B/T ratio.
- (ii) Most of E-SDGs have Sérsic indexes $n > 2$ that increases with B/T ratio in agreement with observations (Fisher & Drory 2008) although there is not a clear correlation. Furthermore, we find that galaxies with larger B/T ratios are more massive and have older SPs.
- (iii) E-SDGs follow scaling relations such as the FJR and FP, in agreement with observations (Cappellari et al. 2013a,b). Regarding the size-mass relation, there is also a reasonable agreement with observations, although E-SDGs with lower B/T ratios tend to be more extended.
- (iv) By analysing the relation between shape and kinematics, we agree with Emsellem et al. (2011), who report that a significant fraction of ETGs tend to be fast rotators. The relations between shape and kinematics indicators are consistent with observations from ATLAS^{3D}. We find a trend for more prolate E-SDGs to have older SPs and to be slower rotators in agreement with observations.
- (v) The MGHs of the E-SDGs suggest different assembly histories according to the stellar mass of the galaxies. In general, there is a large variety of MGHs for the galaxies analysed in this work and in many of them there are signals of mergers and starbursts. E-SDGs with stellar masses in the range $10^{10.5}M_{\odot} < M_{\text{Star}} < 10^{11.2}M_{\odot}$ have MGHs consistent with almost coeval SPs, with a slight trend for the inner regions to be ~ 0.5 Gyr younger than the outskirts. E-SDGs with $B/T > 0.7$ show a slightly stronger signal for outside-in formation. For less massive galaxies there is an increasing contribution of younger SPs within the $0.5 R_{\text{hm}}$, which translates into an age gap measured between the median age of the inner SPs and that of the outer regions. The age gap increases from ~ 0.5 Gyr for the most massive analysed E-SDGs to ~ 2 Gyr for the smallest ones. The outside-in assembly of ETGs with $M_{\text{Star}} < 10^{10.5}M_{\odot}$ is in tension with current observational findings.
- (vi) We find that, at a given median [Fe/H], more massive and older E-SDGs have higher [O/Fe] abundances. E-SDGs with $M_{\text{Star}} < 10^{10}M_{\odot}$ determine a U-shape relation showing a larger variety of chemical abundances in [Fe/H] vs [O/Fe]. The outside-in scenario is consistent with the chemical abundances estimated for SPs at different radial distances. The larger values of [O/Fe] in the outer regions are consistent with stars formed in short starbursts so that the gas could not have been enriched with iron due to SNIa. This trend supports the suggestion that part of the outer stellar enveloped is formed by accreted material. On the other hand the slightly younger stars with lower [O/Fe] in the inner regions indicates that they might have formed from pre-enriched gas.

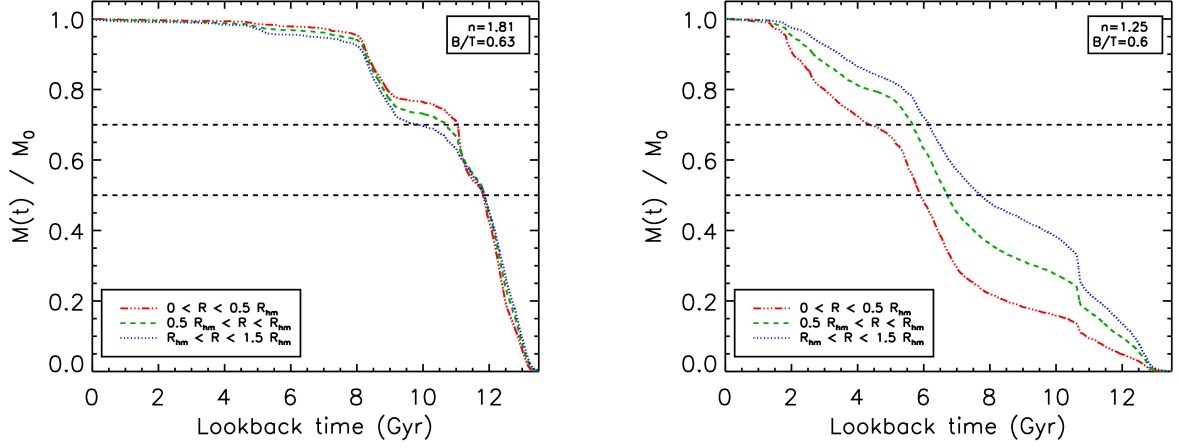


Fig. 12. Top panels: MGHs for two E-SDGs showing different assembly histories: an inside-out (left panel) and an outside-in (right panel). These E-SDGs have similar B/T ratios.

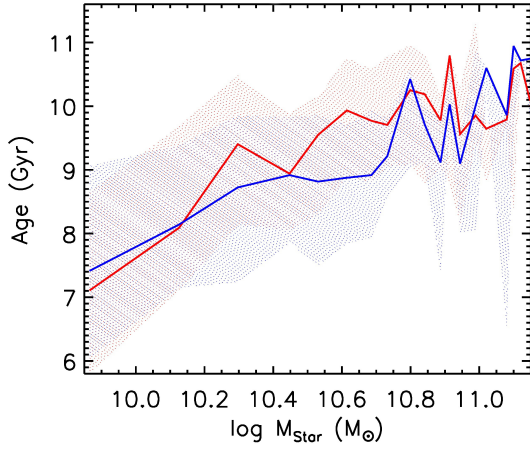


Fig. 13. Median stellar ages for the bulge (red lines) and disc (blue lines) components as a function of galaxy stellar mass for E-SDGs. The shaded regions represent the first and third quartiles.

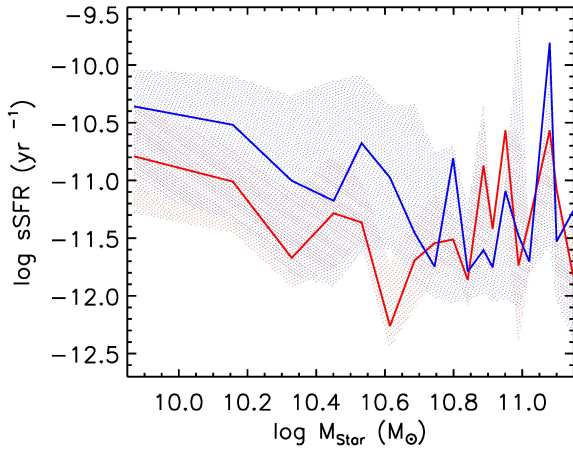


Fig. 14. Median sSFR for the bulge (red line) and the disc (blue line) as a function of galaxy stellar mass for the E-SDGs. Shaded regions depict the first and third quartiles.

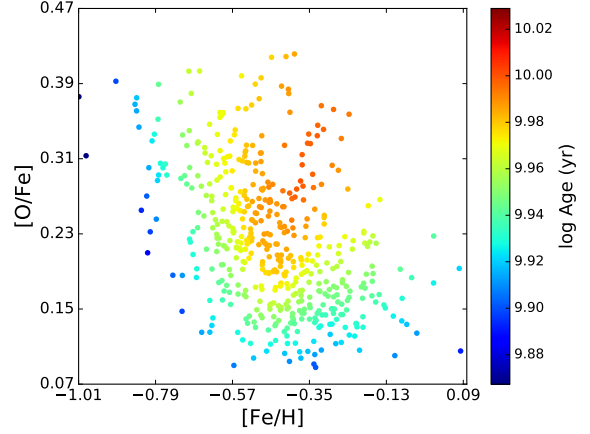


Fig. 15. Distribution of $[O/Fe]$ and $[Fe/H]$ for the E-SDGs coloured according to the median ages of the total SPs. See Appendix B for the non-smoothed distribution.

- (vii) As mentioned before, all selected E-SDGs have a disc component, even if it represents a small fraction of the total mass. The disc concentrates most of the star formation activity which is preferentially located in the central regions. This is not the case for those galaxies dominated by discs. We find that E-DDG (i.e. $B/T < 0.5$) to show a clear ordered MGHs consistent with an inside-out scenario. Hence, galaxies that reach $z = 0$ as spiral galaxies have managed to grow orderly in an inside-out fashion (see Appendix A). We speculate that the following mechanisms could have played a role at modulating the assembly of ETGs. On one hand, the existence of discs in the E-SDGs makes them more susceptible to the effects of secular evolution that can drive gas inflows and feed SF in the central region. AGN feedback might be also needed to act in smaller galaxies (Argudo-Fernández et al. 2018). On the other hand, considering the results of Clauwens et al. (2018) that showed a contribution of ex-situ stars at $r > 5$ kpc, ranging from 10 to 60 per cent, depending on galaxy mass, it might be possible that the accretion of satellites in the outer regions works to enhance the outside-in formation trend as they would

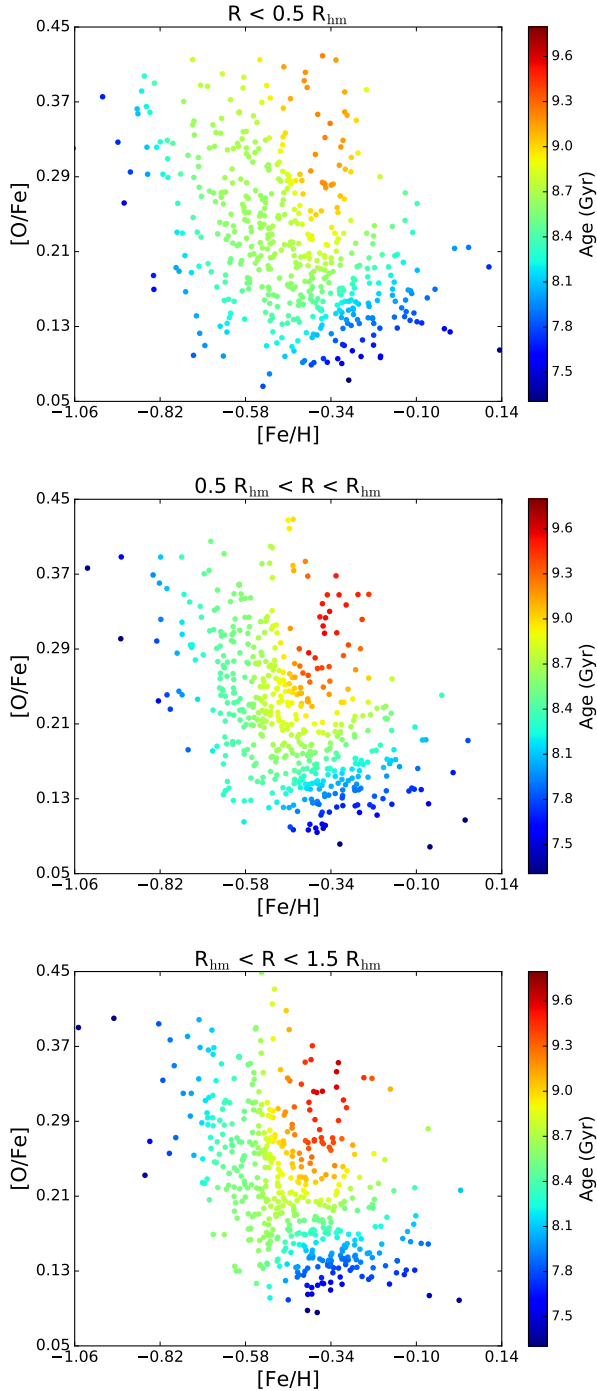


Fig. 16. Distribution of [O/Fe] and [Fe/H] within each radial bin. Symbols are coloured according to mean ages. See Appendix B for the non-smoothed distribution.

contribute with old stars. These minor mergers could also play a role at destabilising an existing disc component.

Acknowledgements. PBT acknowledges partial support from Fondecyt 1150334 (Conicyt). The use of RAGNAR cluster funded by Fondecyt 1150334 and UNAB is acknowledged. This project has received funding from the European Union Horizon 2020 Research and Innovation Programme under the Marie Skłodowska-Curie grant agreement No 734374. This work used the DiRAC Data Centric system at Durham University, operated by the Institute for Computational Cosmology on behalf of the STFC DiRAC HPC Facility (www.dirac.ac.uk). This equipment was funded by BIS National E-infrastructure capital grant ST/K00042X/1, STFC capital grants ST/H008519/1 and ST/K00087X/1, STFC DiRAC Operations grant ST/K003267/1 and Durham

University. DiRAC is part of the National E-Infrastructure. We acknowledge PRACE for awarding us access to the Curie machine based in France at TGCC, CEA, Bruyeres-le-Chatel.

References

- Argudo-Fernández, M., Lacerna, I., & Duarte Puertas, S. 2018, ArXiv e-prints [arXiv:1806.02369]
- Avila-Reese, V., Zavala, J., & Lacerna, I. 2014, MNRAS, 441, 417
- Bernardi, M., Meert, A., Vikram, V., et al. 2014, MNRAS, 443, 874
- Brooks, A. & Christensen, C. 2016, Galactic Bulges, 418, 317
- Bundy, K., Bershady, M. A., Law, D. R., et al. 2015, ApJ, 798, 7
- Bustamente, S. 2018, in Galaxy Interactions and Mergers Across Cosmic Time, 47
- Cappellari, M. 2016, ARA&A, 54, 597
- Cappellari, M., Emsellem, E., Krajnović, D., et al. 2011, MNRAS, 413, 813
- Cappellari, M., McDermid, R., Alatalo, K., et al. 2013a, MNRAS, 432, 1709
- Cappellari, M., McDermid, R. M., Alatalo, K., et al. 2013b, MNRAS, 432, 1862
- Chabrier, G. 2003, PASP, 115, 763
- Clauwens, B., Schaye, J., Franx, M., & Bower, R. G. 2018, MNRAS, 478, 3994
- Cleveland, W. S. & Devlin, S. J. 1988, Journal of the American Statistical Association, 83, 596
- Correa, C. A., Schaye, J., & Trayford, J. W. 2018, ArXiv e-prints [arXiv:1810.07189]
- Crain, R. A., Schaye, J., Bower, R. G., et al. 2015, MNRAS, 450, 1937
- Croom, S. M., Lawrence, J. S., Bland-Hawthorn, J., et al. 2012, MNRAS, 421, 872
- Dalla Vecchia, C. & Schaye, J. 2012, MNRAS, 426, 140
- De Rossi, M. E., Theuns, T., Font, A. S., & McCarthy, I. G. 2015, MNRAS, 452, 486
- Djorgovski, S. & Davis, M. 1987, ApJ, 313, 59
- Dressler, A., Lynden-Bell, D., Burstein, D., et al. 1987, ApJ, 313, 42
- Dubois, Y., Peirani, S., Pichon, C., et al. 2016, MNRAS, 463, 3948
- Emsellem, E., Cappellari, M., Krajnović, D., et al. 2011, MNRAS, 414, 888
- Faber, S. & Jackson, R. 1976, ApJ, 204, 668
- Faber, S. M., Dressler, A., Davies, R. L., Burstein, D., & Lynden-Bell, D. 1987, in Nearly Normal Galaxies. From the Planck Time to the Present, ed. S. M. Faber, 175–183
- Falcón-Barroso, J. & Knapen, J. 2012, Secular Evolution of Galaxies, Canary Islands Winter School of Astrophysics (Cambridge University Press)
- Fisher, D. B. & Drory, N. 2008, AJ, 136, 773
- Gadotti, D. A. 2009, MNRAS, 393, 1531
- Genel, S., Fall, S. M., Hernquist, L., et al. 2015, ApJ, 804, L40
- Genel, S., Nelson, D., Pillepich, A., et al. 2018, MNRAS, 474, 3976
- Gibson, B. K., Pilkington, K., Brook, C. B., Stinson, G. S., & Bailin, J. 2013, A&A, 554, A47
- Hernquist, L. 1989, Nature, 340, 687
- Ibarra-Medel, H. J., Sánchez, S. F., Avila-Reese, V., & Hernández-Toledo, H. M. 2016, MNRAS, 463, 2799
- Kormendy, J. 2016, Galactic Bulges, 418, 431
- Lagos, C. d. P., Schaye, J., Bahé, Y., et al. 2018, MNRAS, 476, 4327
- Li, C., Wang, E., Lin, L., et al. 2015, ApJ, 804, 125
- Lin, L., Zou, H., Kong, X., et al. 2013, ApJ, 769, 127
- McAlpine, S., Bower, R. G., Rosario, D. J., et al. 2018, MNRAS, 481, 3118
- Mihos, J. C. & Hernquist, L. 1996, ApJ, 464, 641
- Mosleh, M., Williams, R. J., & Franx, M. 2013, ApJ, 777, 117
- Naab, T. 2013, in IAU Symposium, Vol. 295, The Intriguing Life of Massive Galaxies, ed. D. Thomas, A. Pasquali, & I. Ferreras, 340–349
- Pedrosa, S. E. & Tissera, P. B. 2015, A&A, 584, A43
- Perez, J., Valenzuela, O., Tissera, P. B., & Michel-Dansac, L. 2013, MNRAS, 436, 259
- Planck Collaboration, Ade, P. A. R., Aghanim, N., et al. 2014a, A&A, 571, A1
- Planck Collaboration, Ade, P. A. R., Aghanim, N., et al. 2014b, A&A, 571, A16
- Rosas-Guevara, Y. M., Bower, R. G., Schaye, J., et al. 2015, MNRAS, 454, 1038
- Rosito, M. S., Pedrosa, S. E., Tissera, P. B., et al. 2018, A&A, 614, A85
- Rupke, D. S. N., Kewley, L. J., & Barnes, J. E. 2010, ApJ, 710, L156
- Sáiz, A., Domínguez-Tenreiro, R., Tissera, P. B., & Courteau, S. 2001, MNRAS, 325, 119
- Salpeter, E. E. 1955, ApJ, 121, 161
- Sánchez, S. F., Kennicutt, R. C., Gil de Paz, A., et al. 2012, A&A, 538, A8
- Sánchez-Blázquez, P., Forbes, D. A., Strader, J., Brodie, J., & Proctor, R. 2007, MNRAS, 377, 759
- Schaye, J., Crain, R. A., Bower, R. G., et al. 2015, MNRAS, 446, 521
- Schaye, J. & Dalla Vecchia, C. 2008, MNRAS, 383, 1210
- SDSS Collaboration, Albareti, F. D., Allende Prieto, C., et al. 2016, ArXiv e-prints [arXiv:1608.02013]
- Sérsic, J. L. 1968, Atlas de galaxias australes

- Sillero, E., Tissera, P. B., Lambas, D. G., & Michel-Dansac, L. 2017, MNRAS, 472, 4404
- Taylor, P. & Kobayashi, C. 2017, MNRAS, 471, 3856
- Tissera, P. B. 2000, ApJ, 534, 636
- Tissera, P. B. 2012, Boletín de la Asociación Argentina de Astronomía La Plata Argentina, 55, 233
- Tissera, P. B., Machado, R. E. G., Sanchez-Blazquez, P., et al. 2016, A&A, 592, A93
- Tissera, P. B., Rosas-Guevara, Y., Bower, R. G., et al. 2018, ArXiv e-prints [arXiv:1806.04575]
- Tissera, P. B., White, S. D. M., Pedrosa, S., & Scannapieco, C. 2010, MNRAS, 406, 922
- Tissera, P. B., White, S. D. M., & Scannapieco, C. 2012, MNRAS, 420, 255
- Trayford, J. W., Frenk, C. S., Theuns, T., Schaye, J., & Correa, C. 2018, ArXiv e-prints [arXiv:1805.03210]
- van de Sande, J., Scott, N., Bland-Hawthorn, J., et al. 2018, Nature Astronomy, 2, 483
- Vincenzo, F., Kobayashi, C., & Taylor, P. 2018, MNRAS, 480, L38
- Wang, J., Kauffmann, G., Overzier, R., et al. 2011, MNRAS, 412, 1081
- Wiersma, R. P. C., Schaye, J., & Smith, B. D. 2009, MNRAS, 393, 99
- Zavala, J., Avila-Reese, V., Firmani, C., & Boylan-Kolchin, M. 2012, MNRAS, 427, 1503
- Zavala, J., Frenk, C. S., Bower, R., et al. 2016, MNRAS, 460, 4466

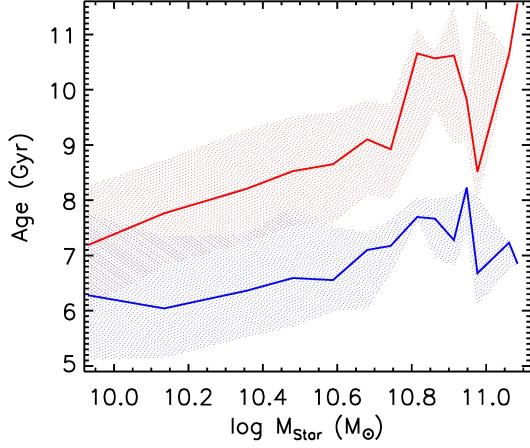


Fig. A.1. Median stellar ages for the bulge (red lines) and disc (blue lines) components as a function of galaxy stellar mass for DDGs. The shadowed regions represent the first and third quartiles.

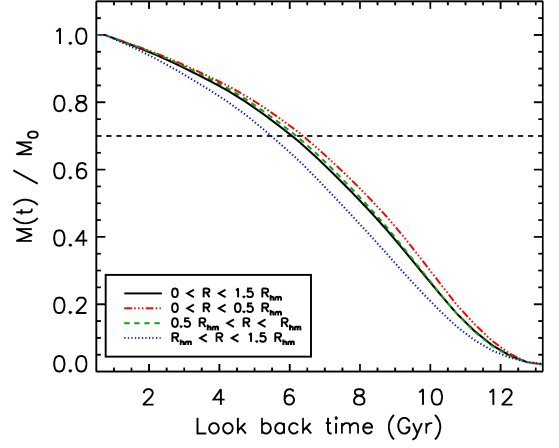


Fig. A.2. Average global and radial normalised MGH for the DDGs. It presents a clear inside-out growth.

Appendix A: Comparison with the disc-dominated galaxies

For comparison purposes, we also analyse some of the relations studied in the main section for all galaxies resolved with more than 10000 particles. This sample comprises 70 per cent of E-DDGs and 30 per cent of E-SDGs.

In Section 4, we emphasise the fact that SDGs in the EAGLE simulation tend to show an outside-in growth. However as expected this is not the case for DDGs. The inside-out scenario is consistent with previous analysis of the EAGLE simulations (Zavala et al. 2016; Tissera et al. 2018). While no significant differences between the mean ages of the bulge and disc components of E-SDGs are found (section 4), in the DDGs bulges are older than discs by about ~ 2 Gyr (Fig. A.1). The average global and radial MGHs for DDGs can be seen in Fig. A.2. The 70 per cent of the stellar mass in the inner, intermediate and outer radial intervals is attained at lookback times of 6.5 Gyr, 6 Gyr and 5.5 Gyr, respectively.

In Section 4 we find the sSFR of disc and bulge components of E-SDGs are similar. However, when all galaxies in the sample regardless of the B/T ratios are considered a trend for higher B/T ratio to have the lower sSFR as shown in Fig. A.3.

We remark that in these plots we did not fix the colorbar limits to the first and third quartiles of the variable according to which we colour the symbols. Instead we use a wider range. The reason for this is that most of the galaxies in our sample are DDGs, and therefore have B/T lower than 0.5.

Appendix B: Non-smoothed distributions

In this Appendix we show the scatter plots of the figures analysed in Sections 3 and 4 without applying the smoothing method of Cappellari et al. (2013b) in order to provide a mean to assess the real distributions.

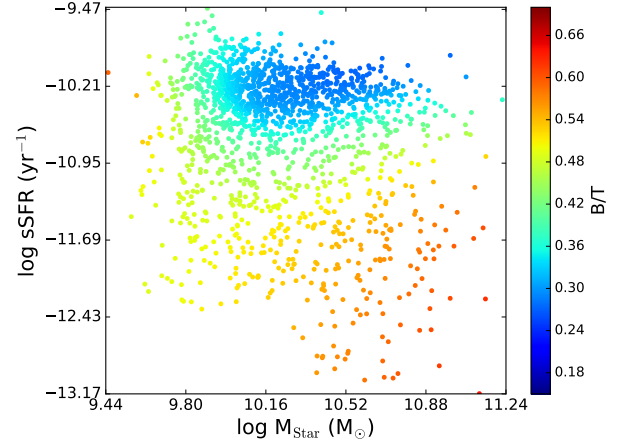


Fig. A.3. sSFR as a function of stellar mass of the total analysed sample. Symbols are coloured according to the B/T ratio. See Appendix B for the non-smoothed distribution.

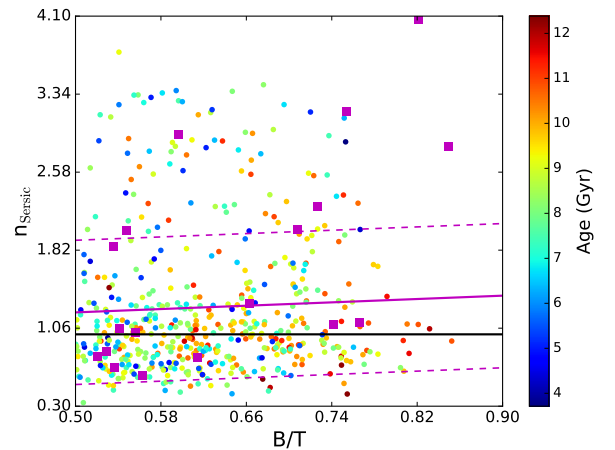


Fig. B.1. The Sérsic index (n_{Sersic}) as a function of B/T ratio for the simulated E-SDGs, coloured according to the mass-weighted average age of the galaxy stellar mass. A linear regression fit is included (magenta solid line) with its 1σ dispersion (magenta dashed line). For comparison, we also include the results by Rosito et al. (2018) (magenta squares). The line $n_{\text{Sersic}} = 1$ is depicted in a black line.

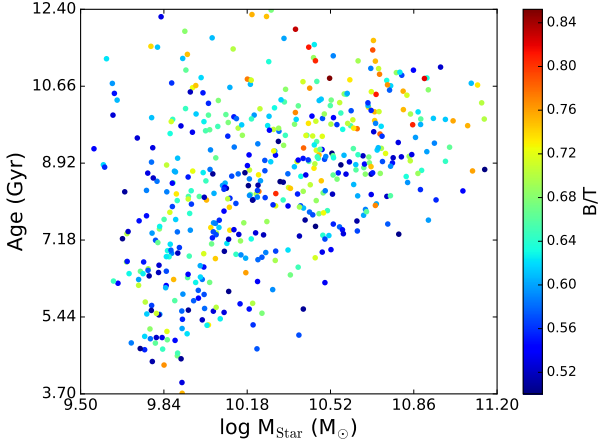


Fig. B.2. Mass-weighted average stellar age of the E-SDGs (i.e. bulge and disc SPs) as a function of stellar mass for the simulated galaxies. The symbols are coloured according to the B/T ratios.

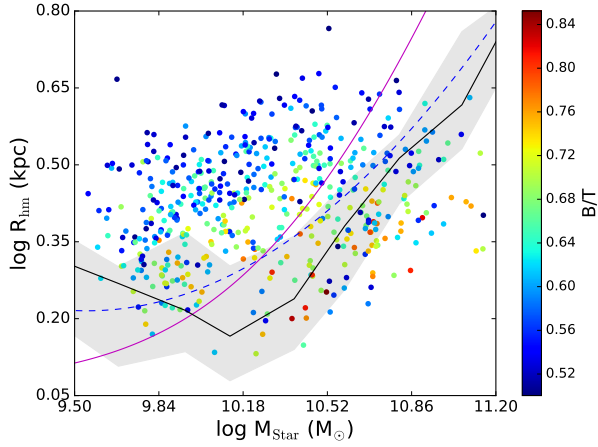


Fig. B.3. The mass-size relation estimated for the E-SDGs. Symbols are coloured according to their B/T ratio. The median of the observations from ATLAS^{3D} (black line; the first and third quartiles are shown as shadowed region) and the observed relations for ETGs reported by Mosleh et al. (2013, magenta solid line) and Bernardi et al. (2014, blue dashed line) are included for comparison.

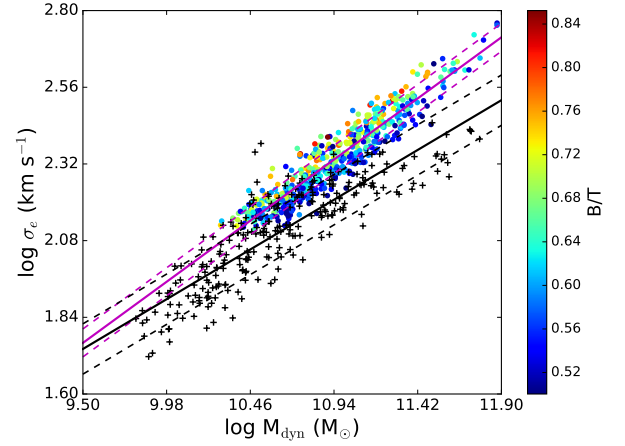
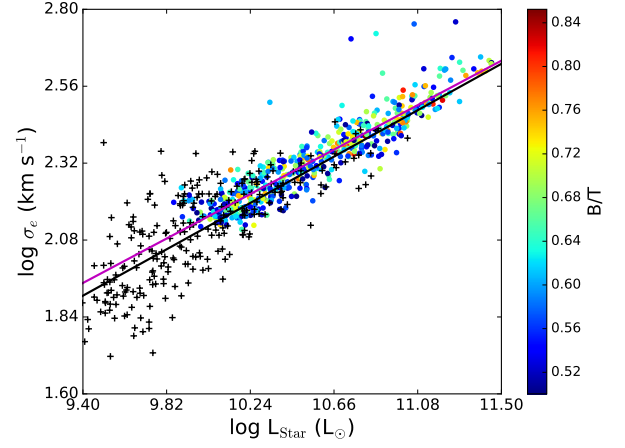


Fig. B.4. FJR for simulated E-SDGs (filled circles) and observed ETGs from ATLAS^{3D} (black crosses) galaxies. The upper panel shows the FJR as a function of luminosity and the lower panel as a function of M_{dyn} . The E-SDGs are coloured according to their B/T ratios. The best-fitted linear regressions for the E-SDGs (magenta line) and for the observations (black line) are included.

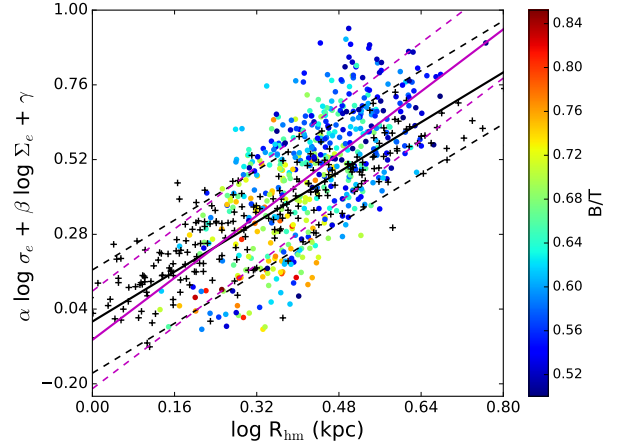


Fig. B.5. The FP for the simulated SDGs calculated with the parameters estimated for the ATLAS^{3D} sample. E-SDGs are also depicted according to their B/T ratio. The black line denotes the one-to-one relation and the magenta line represents the best fit for the E-SDGs. In dashed lines we show the rms corresponding to the least squared regression and the one-to-one relation.

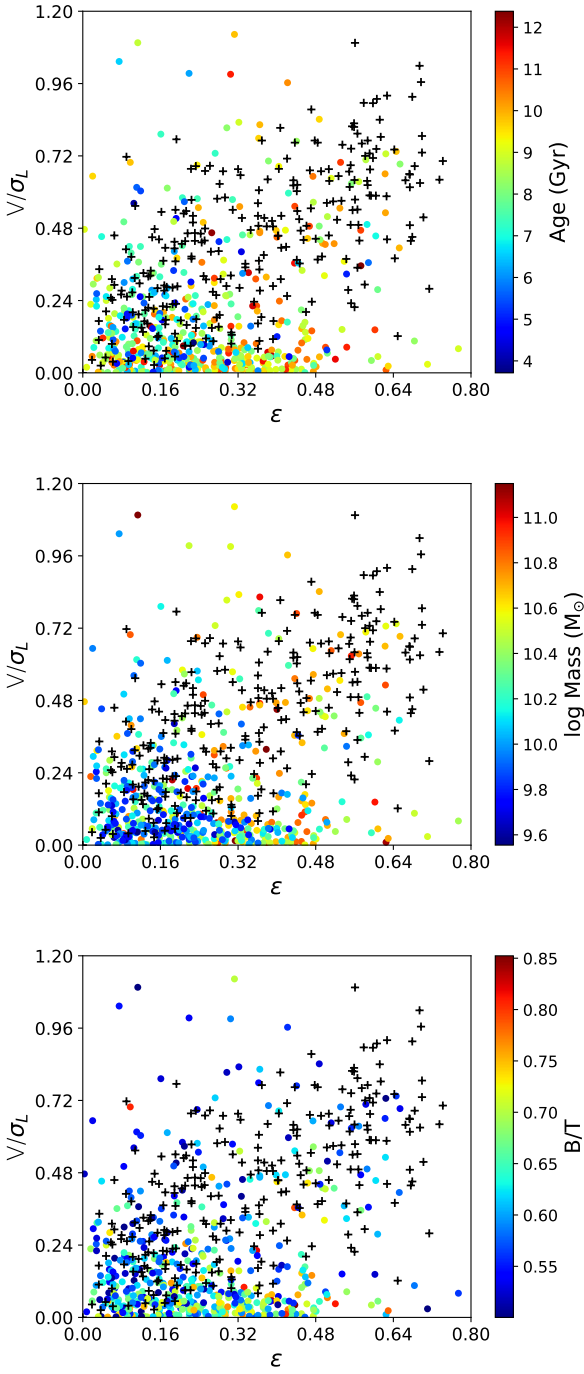


Fig. B.6. Anisotropy diagram for the E-SDGs. E-SDGs are coloured according to mass-weighted average age (top panel), stellar mass (middle panel) and B/T ratio (bottom panel). Observational data from ATLAS^{3D} are also shown (Emsellem et al. 2011, black crosses).

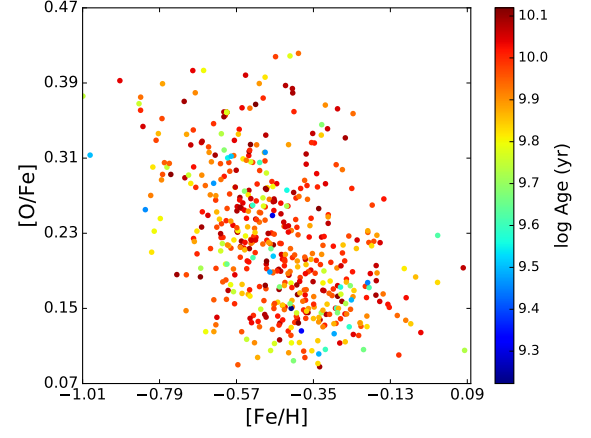


Fig. B.7. Distribution of $[O/Fe]$ and $[Fe/H]$ for the E-SDGs coloured according to the median ages of the total SPs.

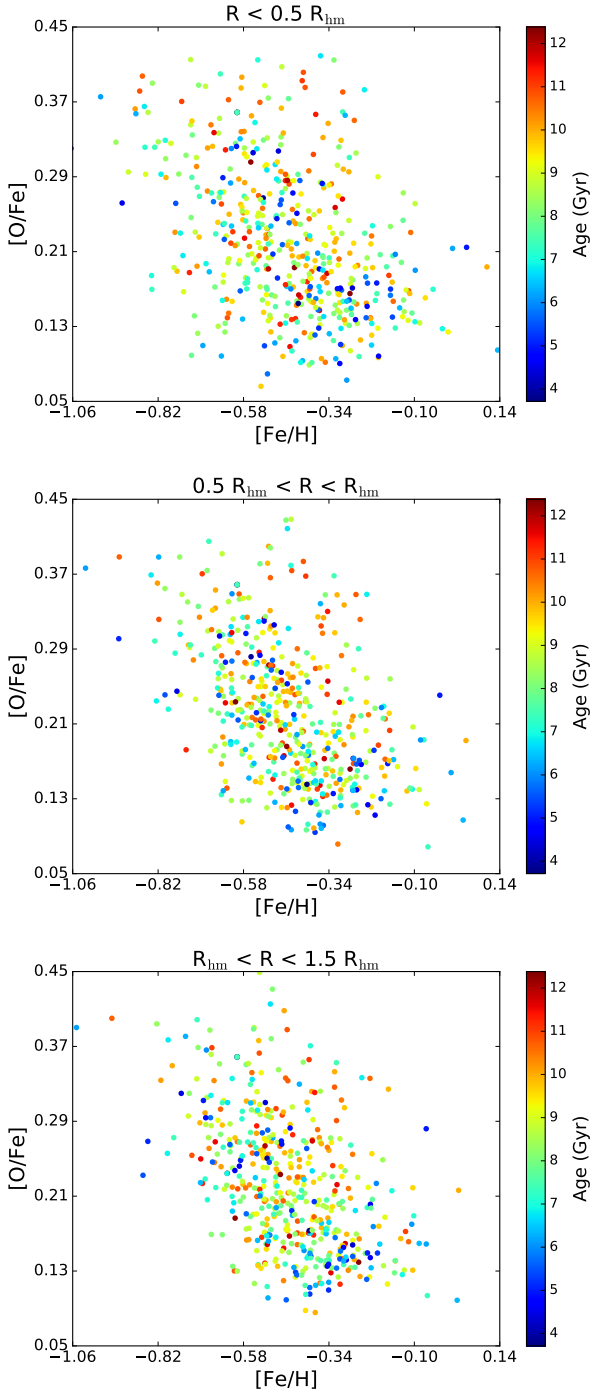


Fig. B.8. Distribution of [O/Fe] and [Fe/H] within each radial bin. Symbols are coloured according to mean ages.

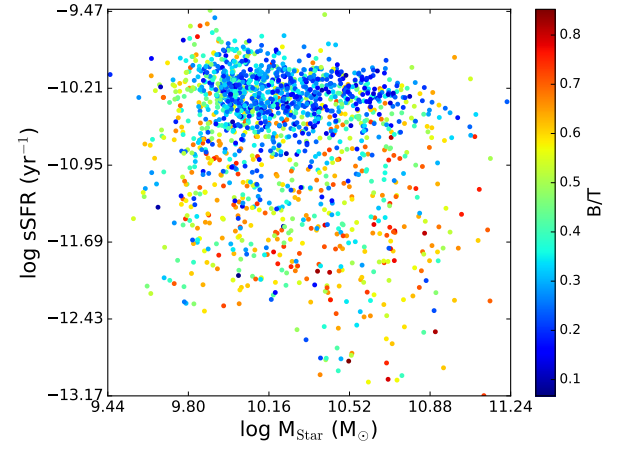


Fig. B.9. sSFR as a function of stellar mass of the total analysed sample. Symbols are coloured according to the B/T ratio.